Probing a Two-Level System Bath via the Frequency Shift of an Off-Resonantly Driven Cavity

Thibault Capelle,[1,*] Emmanuel Flurin,[2] Edouard Ivanov,[1] Jose Palomo,[2] Michael Rosticher,[2] Sheon Chua,[1] Tristan Briant,[1] Pierre-François Cohadon,[1] Antoine Heidmann,[1] Thibaut Jacqmin,[1] and Samuel Deléglise[1]

[1] *Laboratoire Kastler Brossel, Sorbonne Université, CNRS, ENS-Université PSL, Collège de France, 75005 Paris, France*

[2] *Département de Physique, ENS-Université PSL, CNRS, 24 rue Lhomond, F-75005 Paris, France*

(Received 19 August 2019; revised manuscript received 23 December 2019; accepted 18 February 2020; published 9 March 2020)

Although the main loss channel of planar microwave superconducting resonators has been identified to be related to an external coupling to a two-level system (TLS) bath, the behavior of such resonators in the presence of an off-resonant pump has yet to be fully understood. Alongside the well-known power-dependent damping, we observe a frequency shift with a conspicuous maximum for intermediate pump power that is attributed to a spectrally asymmetric saturation of the TLSs. We derive a semiclassical model that describes both of these effects quantitatively. The model is validated experimentally by performing a two-tone spectroscopy of several resonators fabricated on various substrates. Together with the provided analytic formulas, the technique proposed here is a simple yet powerful tool to unambiguously identify the presence of a limiting TLS bath, and to characterize various properties thereof, such as its average dephasing rate.

DOI: 10.1103/PhysRevApplied.13.034022

I. INTRODUCTION

Microwave superconducting resonators are an ubiquitous resource in various quantum devices, ranging from kinetic inductance bolometers [1,2] and parametric amplifiers [3,4], to embedded circuits for cavity quantum electrodynamics [5–7]. In addition, they play a central role as a microwave interface in hybrid quantum systems such as solid-state spins [8], mechanical resonators [9,10], and ferromagnetic magnons [11,12]. Owing to the very low resistivity of superconducting materials, combined with advanced electromagnetic engineering to reduce radiation losses, the dominant loss channel of such resonators is the dielectric loss due to the presence of a two-level system (TLS) bath in amorphous materials [13]. A salient feature of this loss mechanism is its nonlinear nature. Indeed, the damping of TLS-limited cavities is shown to depend on resonator occupancy, originating from thermal fluctuations [14], from resonant excitation [15,16], or from nondegenerate resonant-mode occupancy [17,18]. The characterization of the microscopic properties of individual TLSs probed under stress [19] or dc voltage bias [20] is an active field of research, and considerable experimental efforts have been devoted to the characterization [21–23] and mitigation [24–28] of TLS-related losses for superconducting resonators in the single-photon regime. In many applications, however, strong microwave tones are applied with significant frequency detuning from the resonance frequency in order to activate a parametric interaction between the resonator mode and various degrees of freedom, such as a mechanical resonator [9], an auxiliary microwave cavity [29], or a superconducting qubit [30]. In this configuration, the off-resonant microwave tone responsible for the saturation of the TLS bath is spectrally distinct from the resonant mode subjected to the losses, simultaneously giving rise to a shift of the resonance frequency and a modification of the population dependence of the quality factor.

In this paper, we propose a scheme to probe the energy relaxation and frequency-shift properties of an off-resonantly driven microwave cavity due to the presence of a TLS bath. A semiclassical model that describes the modified susceptibility is derived and compared to experimental data obtained on several resonators fabricated on different substrates. Contrary to earlier works where a pump tone was injected at resonance with specifically engineered cavity modes [17,18], our technique is readily applicable to any kind of resonator, which makes it a versatile approach to identify a TLS loss mechanism, and quantify its contribution to the total resonator loss, a key capability for the design and optimization of high-Q cavities. Moreover, the ability to continuously scan the pump detuning

*thibault.capelle@lkb.upmc.fr

allows us to determine the average dephasing rate of the TLS bath by relating it to a well-controlled experimental parameter.

The paper is organized as follows: in Sec. II, we describe the lumped-element resonators on which the measurements have been conducted. We then present in Sec. III the two-tone characterization scheme, and discuss a distinctive feature of this pump-probe technique: a pump-induced frequency shift of the resonator's frequency. In Sec. IV, we propose a semiclassical model that accounts for the modified susceptibility of a microwave resonator due to the presence of a pump tone, and investigate numerically the validity of this model. Finally, in Sec. V, we summarize the results obtained by fitting our model on various datasets obtained with different resonators fabricated on three different substrates. Together with the analytical formulas provided in Sec. IV, the proposed two-tone technique constitutes a simple characterization method for the design of superconducting resonators, and an alternative tool for the investigation of amorphous materials.

II. SAMPLE DESIGN AND FABRICATION

Our samples are compact resonators, made of a meander inductor in parallel to an interdigitated capacitor with a tooth period as small as 1 μm (see Fig. 1). These resonators have been initially optimized to maximize the coupling of the microwave mode to an external degree of freedom such as localized emitters [31,32] or the motion of a planar dielectric membrane placed in the evanescent field of the circuit via dielectric gradient forces [33]. Due to the evanescent profile of the electric field around the interdigitated capacitor [34], the electric field is strongly confined in the direction transverse to the electrode plane. As a concomitant effect, the participation ratio of the surface interfaces and any deposited dielectric layers is thus enhanced in this geometry, which leads to an intentionally larger TLS signal in the form of resonator frequency shift and damping. Microwave radiation is coupled in and out of the resonator with a coplanar-waveguide feedline inductively coupled to the resonator.

To test the ability of our technique to discriminate between the properties of various dielectric materials, we fabricate resonators on three different substrates: a 250-μm-thick substrate of float-zone- (FZ) grown (100) intrinsic silicon, with a resistivity of more than 10 000 Ω cm (substrate referred to as Si), 500-μm-thick substrate of FZ-grown (100) *P*-doped type-*n* silicon, with a resistivity of more than 10 000 Ω cm, with 2 μm of SiO_2 from thermal oxidation (substrate referred to as Si/SiO_2), and finally, a 650-μm-thick substrate of Czochralski- (CZ) grown (100) silicon, with *P*/boron doping and a resistivity of 1–30 Ω cm, with 200 nm of Si_3N_4 deposited through low-pressure chemical vapor deposition (substrate referred to as Si/Si_3N_4).

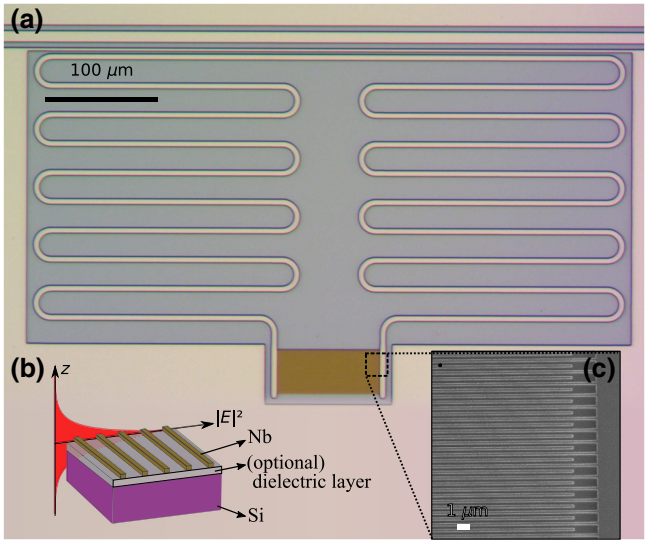

FIG. 1. (a) Optical micrograph of the microwave cavity. (b) Dielectric environment of the capacitor and profile of the electric field mode profile (magnitude square), which exhibits, in good approximation, an exponentially decaying z dependence. Silicon is represented in purple, niobium is represented in gray, and the optional (SiO_2 or Si_3N_4) amorphous dielectric layer is represented in green. (c) View of the capacitor using electron microscopy.

The resonators are fabricated via e-beam lithography on a 100-nm-thick niobium layer evaporated using a Plassys system under ultra-high vacuum (approximately equal to 5×10^{-10} mbar). For each substrate, ten resonators are multiplexed on the same coupling waveguide and their resonance frequency is staggered by incrementing the capacitor's area by steps approximately equal to 2.5%. The coupling-limited quality factor is designed to be approximately equal to 2×10^4.

III. PUMP-PROBE CHARACTERIZATION

Each sample is placed in a ^{3}He cryostat with a 330-mK base temperature, and probed by a two-tone excitation [see Fig. 2(a)]: a strong pump with a fixed detuning in an interval spanning from several linewidths below to several linewidths above the cavity resonance, saturates the TLS bath and a weak probe is used to measure the resonance frequency ω_c and damping Γ_{tot} of the resonator [see Fig. 2(b)]. An example of the complex probe transmission $\mathcal{T}$ recorded for various pump power is represented in Fig. 2(c). Using a fit formula [35,36] that properly takes into account the effect of standing waves in the coupling waveguide, we can separate the contributions of the coupling waveguide Γ_{ext} and internal damping Γ_{int} in the total cavity linewidth $\Gamma_{\text{tot}} = \Gamma_{\text{int}} + \Gamma_{\text{ext}}$.

Figure 3(a) shows the frequency shift $\Delta\omega_c$ and internal damping Γ_{int} measured by the probe for various pump

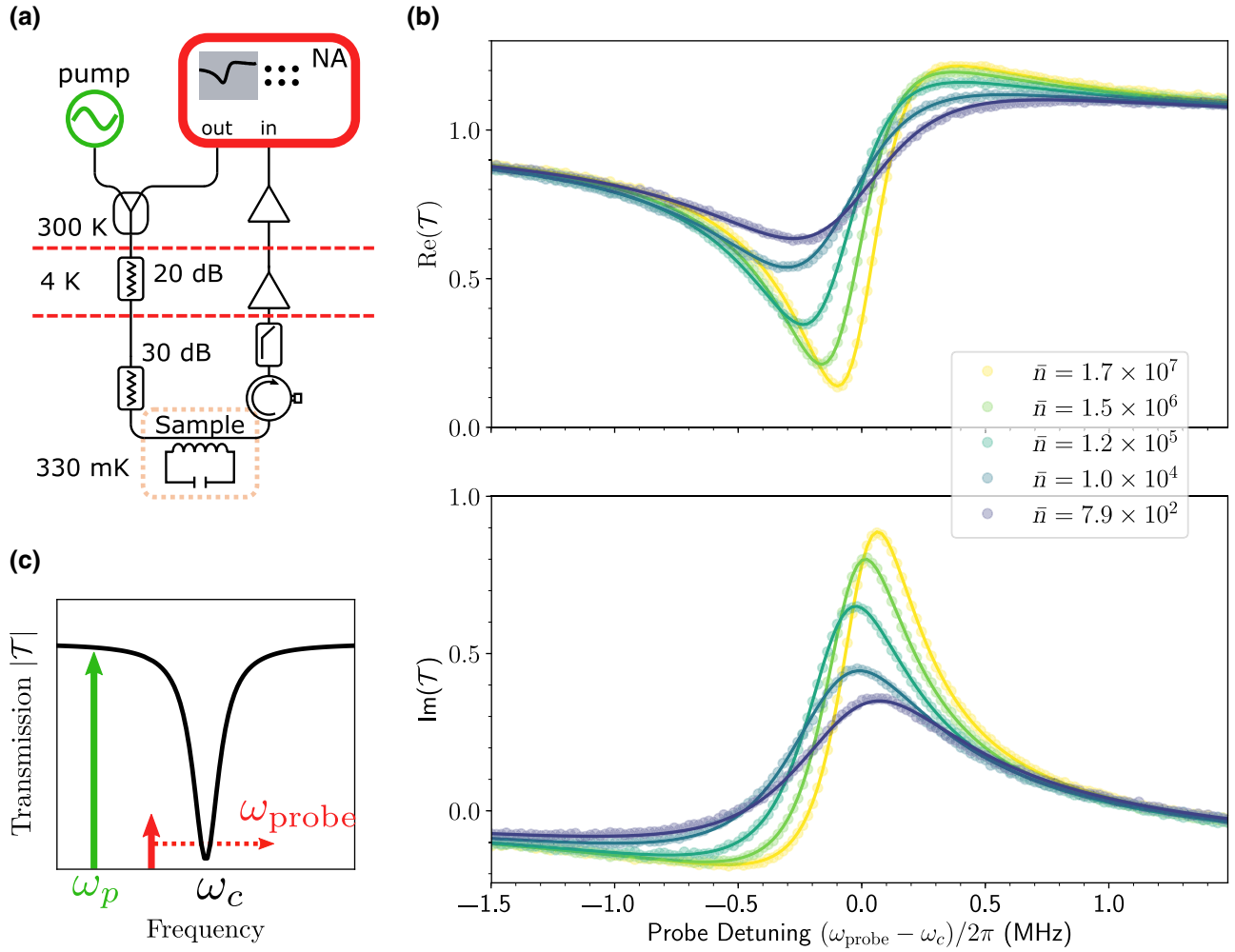

FIG. 2. (a) Experimental setup: the output of a network analyzer (probe) is combined with that of a signal generator (pump) to drive the sample placed in a ^{3}He cryostat. NA, network analyzer. (b) Experimental protocol: a strong pump field is applied with a given detuning from a microwave cavity resonance, while a weak probe field is swept across the cavity resonance to measure its transmission spectrum $\mathcal{T}$. (c) Real (top) and imaginary part (bottom) of the probe transmission for a pump detuning of 4 MHz at various (pump) intracavity photon numbers.

powers and detunings Δ. Even with the large pump detuning, we observe a decrease of the resonator losses for increasing pump power. This effect can be attributed to the saturation of the TLS bath by the intracavity pump tone. To deconvolve the filtering of the detuned incoming pump tone by the cavity linewidth, the pump power is converted into intracavity photon number $\bar{n}$ via the formula $\bar{n} = 2\Gamma_{\rm ext}|a_{\rm in}|^2/(\Gamma_{\rm tot}^2 + 4\Delta^2)$, where $|a_{\rm in}|^2$ is the incoming photon flux in photon/s as determined by an independent calibration experiment (see Appendix C). Furthermore, to measure the correct intrinsic damping at low power, the probe beam is ensured to be sufficiently weak to prevent it from saturating the TLS bath.

A noticeable feature of this pump-probe experiment is the pump-dependent frequency shift observed in Fig. 3(a). This result is in contrast with single-tone experiments where the interaction with the TLS bath is only affecting the resonator damping. Moreover, the observed frequency shift has a nonmonotonous behavior, with a maximum (respectively, minimum) resonator frequency observed for a given pump power at positive (respectively, negative) pump detuning Δ.

In the next section, we give a detailed theoretical description of the pump-probe experiment, and we propose an analytical model that can be used to link the previous experimental signatures with various properties of the bath, such as the average TLS dephasing rate.

IV. THEORETICAL ANALYSIS

Here, we derive analytical formulas for the frequency shift and damping induced by an ideal bath of TLSs. These are characterized by a uniform frequency distribution of density $P_0/2\pi$ (in Hz^{-1}), a coupling g to the resonator

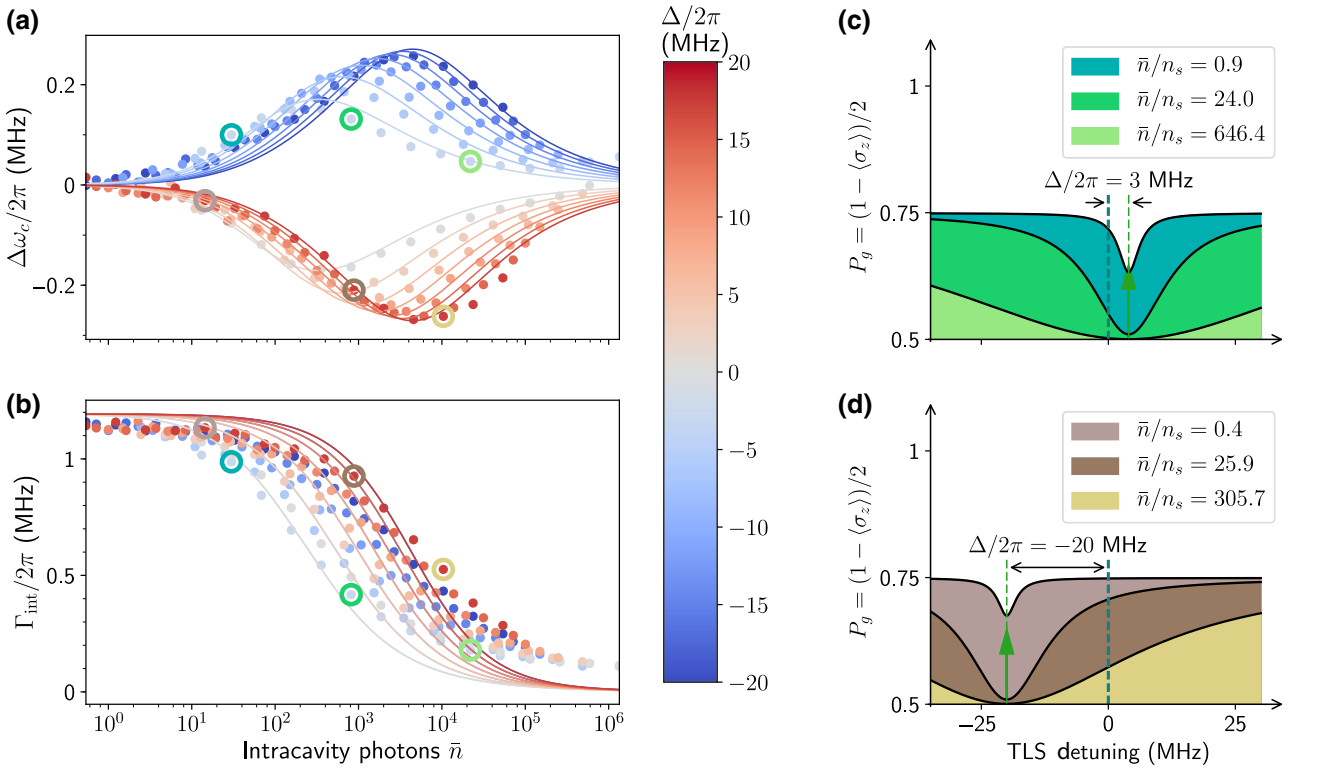

FIG. 3. (a) Frequency shift and (b) damping of the resonator, versus the number of intracavity photons. Each color corresponds to a different pump detuning ranging from −20 to +20 MHz (color bar). Points correspond to experimental data, while solid lines correspond to fits by the model [Eqs. (3) and (4)]. (c),(d) Ground-state population distribution of the TLSs versus their frequency detuning $\omega_q - \omega_c$ calculated with Eq. (1). The various curves have been calculated for various intracavity pump photon numbers and the related points in (a),(b) are highlighted with the corresponding color circles. This measurement is performed on a Si/SiO_2 sample, with $\omega_c/2\pi = 7.521$ GHz (see circled point in Fig. 5).

assumed to be identical for all TLSs in the distribution, and a damping (dephasing) rate Γ_1 (Γ_2). This is a simplifying assumption since the real TLS population has some statistical variation in these parameters (for instance, the coupling g of individual TLSs to the resonator depends on the value and orientation of the electric field at the TLS location). However, by neglecting these effects, we can provide analytical formulas, which are numerically verified in Sec. IV D with a more realistic TLS bath, and found to be in good agreement provided the fitted parameters are interpreted as averaged values over the TLS distribution.

A. Analytical formula for a uniform TLS bath

As the weak probe has a negligible effect on the TLS bath, the pump affects the population imbalance $\langle\boldsymbol{\sigma}_z(\omega_q)\rangle$ according to the saturation law for a TLS at frequency ω_q

$$\langle\boldsymbol{\sigma}_z(\omega_q)\rangle = \langle\boldsymbol{\sigma}_z\rangle_{\rm th}\left[1 - \frac{\Gamma_2^2\bar{n}/n_s}{(\omega_q-\omega_p)^2 + \Gamma_2^2(1+\bar{n}/n_s)}\right], \tag{1}$$

where $\langle\boldsymbol{\sigma}_z\rangle_{\rm th} = -\tanh\left(\hbar\omega_q/2k_BT\right) \approx -0.52$ is the thermal imbalance resulting from the Fermi-Dirac distribution at the base temperature $T = 330$ mK of our ^{3}He cryostat, Γ_2 (Γ_1) the TLS dephasing (energy relaxation) rate, g the coupling rate, $\bar{n}$ the number of intracavity photons, $n_s = \Gamma_1\Gamma_2/4g^2$ the number of photons required to saturate the TLS transition. In turn, the population imbalance $\langle\boldsymbol{\sigma}_z(\omega_q)\rangle$ of a single TLS induces a shift of the complex cavity frequency [18]

$$\delta\omega_c = \frac{g^2\langle\boldsymbol{\sigma}_z(\omega_q)\rangle}{\omega_q - \omega_c + i\Gamma_2}. \tag{2}$$

The frequency shift and damping, as measured by the probe beam, are related to the real and imaginary parts of $\delta\omega_c$. The total frequency shift and damping are obtained by integrating the contribution of individual TLS, assuming a flat spectral distribution of density P_0, uniform coupling rate g, and no interaction between individual TLSs, leading to (see Appendix B)

$$\Delta\omega_c = -\frac{\Gamma_0}{2}\frac{(\Delta/\Gamma_2)\,(\bar{n}/n_s)}{\sqrt{1+\bar{n}/n_s}\left[(\Delta/\Gamma_2)^2 + \left(1+\sqrt{1+\bar{n}/n_s}\right)^2\right]}, \tag{3}$$

$$\Gamma_{\rm int} = \Gamma_0 \left[1 - \frac{\bar{n}/n_s}{\sqrt{1+\bar{n}/n_s}} \frac{1+\sqrt{1+\bar{n}/n_s}}{(\Delta/\Gamma_2)^2 + \left(1+\sqrt{1+\bar{n}/n_s}\right)^2} \right]. \tag{4}$$

In these formulas, in addition to the dephasing rate Γ_2, the TLS bath is described by two characteristic parameters: $\Gamma_0 = P_0 g^2 \left|\langle \boldsymbol{\sigma}_z \rangle_{\rm th}\right|$, the maximum damping produced by the TLS bath at the temperature T, that acts as a scaling factor on the curves $\Delta\omega_c(\bar{n}, \Delta)$ and $\Gamma_{\rm int}(\bar{n}, \Delta)$, and n_s, that corresponds to a scaling of the curves with respect to the axis $\bar{n}$.

Equations (3) and (4) agree well with the experimental observations of the previous section. The solid lines in Figs. 3(a) and 3(b) are a simultaneous fit of the experimental points to Eqs. (3) and (4) with Γ_0, Γ_2, and n_s as free parameters. The small (approximately 5%) discrepancy between the measured damping and the fits at low pump power is attributed to the residual saturation of the TLS bath by the probe tone. We also observe a residual loss at high pump power, that represents approximately 10% of the low-power value and that is attributed to a loss mechanism unrelated to the TLS bath. The smaller overall variation of the measured damping cannot be captured by the model since we perform a common fit on both damping and detuning points. We nonetheless observe a decrease of this discrepancy as the probe power is weakened, consistent with the hypothesis of a residual saturation of the bath by the probe field. Since the detuning curve is not affected by these artifacts, we attribute a 90% weighting to the detuning data in the global fit, and ignore these effects in our model for simplicity. In the following sections, we give a qualitative explanation of the phenomena captured by our model and derive simple formulas in two limiting cases.

B. Small detuning limit

When the pump detuning is small compared to the TLS dephasing rate ($\Delta \ll \Gamma_2$), the TLSs that are affected by the pump are the same as in a single-tone experiment. In particular, since an equal number of TLSs are excited by the pump on either side of the cavity, the frequency shift vanishes in this regime:

$$\Delta\omega_c = 0, \tag{5}$$

$$\Gamma_{\rm int} = \frac{\Gamma_0}{\sqrt{1+\bar{n}/n_s}}. \tag{6}$$

Equation (6) is the well-known power-dependent absorption of the TLS bath derived in the context of single-tone experiments [37].

C. Large detuning limit

In the large detuning limit ($\Delta \gg \Gamma_2$), the effect of the pump field on the TLS distribution is more subtle: as the intracavity field resonates at a frequency ω_p that is significantly different from ω_c, a depletion in population imbalance $\langle \boldsymbol{\sigma}_z(\omega_q) \rangle$ occurs for TLSs that have a frequency ω_q close to ω_p. More quantitatively, the width of this Lorentzian dip is given by the generalized Rabi frequency $\Gamma_2\sqrt{1+\bar{n}/n_s}$. Consequently, the frequency pull exerted by TLSs that are above the cavity frequency will not be perfectly compensated by those that are below, resulting in a net shift of the cavity resonance. At even larger pump power, the width of the dip in population imbalance exceeds the pump detuning, such that the asymmetry decreases. Qualitatively, the maximum cavity frequency shift occurs when the pump creates a depletion of population imbalance $\langle \boldsymbol{\sigma}_z(\omega_q) \rangle$ of spectral width Δ. In the current limit, this occurs when $\bar{n} \approx n_s (\Delta/\Gamma_2)^2$. This effect is illustrated in Figs. 3(c) and 3(d), where the ground-state population is calculated using Eq. (1) for two different pump detunings, and various pump powers spreading below and above this value.

Further, we can note that Eqs. (3) and (4) can be approximated in the large detuning limit by

$$\Delta\omega_c = -\frac{\Gamma_0}{2} \frac{\delta}{\delta^2+1}, \tag{7}$$

$$\Gamma_{\rm int} = \Gamma_0 \frac{\delta^2}{1+\delta^2}, \tag{8}$$

with the dimensionless parameter $\delta = \sqrt{n_s/\bar{n}}\Delta/\Gamma_2$. Hence, in the regime $\Delta \gg \Gamma_2$, the curves $\Delta\omega_c(\bar{n}, \Delta)$ are invariant under the transformation $(\bar{n}, \Delta) \to (\sqrt{\alpha}\bar{n}, \Delta/\alpha)$, where α is an arbitrary positive number. In particular, the maximum frequency shift and damping are independent of the pump detuning provided it greatly exceeds the dephasing rate Γ_2 of the bath and their ratio is a nonadjustable prediction of the model:

$$\frac{\Delta\omega_c(\delta = 1)}{\Gamma_{\rm int}(\bar{n} = 0)} = 1/4. \tag{9}$$

We find experimentally $\max(\Delta\omega_c)/\max(\Gamma_{\rm int}) \approx 0.23$ with the data presented in Figs. 3(a) and 3(b).

By capturing the transition between these two distinct regimes, the fit with the full Eqs. (3) and (4) performs a direct comparison between the TLS bath dephasing rate Γ_2, and the known pump detunings Δ. The two-tone experiments, therefore, give direct experimental access to Γ_2, a parameter that is elusive to the single-tone probing of a TLS bath.

D. Effect of the nonuniform TLS distribution

1. Monte Carlo simulations

The model derived in the previous section is based on the assumption that the bath is composed of a large number of TLSs with identical properties. In this section,

we study numerically how a nonuniform distribution of TLS parameters affects the previous findings. We perform a Monte Carlo simulation where we randomly pick an ensemble of N TLSs characterized by the parameters $\{\omega_{q,i}, g_i, \Gamma_{1,i}, \Gamma_{2,i}\}_{i\in[1,\ldots,N]}$. The individual TLS frequencies $\omega_{q,i}$ are drawn from a uniform distribution of density P_0. The couplings g_i are chosen randomly in a uniform distribution on the intervals $[0, g_{\max}]$: this distribution would be rigorously justified for a bath of TLSs with random orientations in a uniform electric field. The energy damping and dephasing rates $\Gamma_{1,i}$ and $\Gamma_{2,i}$ are drawn from a log-normal distribution, where the standard deviation of the variable's logarithm is fixed to 1/2.

The TLS spectral density P_0 is not constrained by our model, we thus choose a starting value $P_0/2\pi = 1\ \mathrm{kHz}^{-1}$ large enough to ensure that the numerical results are insensitive to the sampling noise associated with the random realization of TLSs. In practice, we choose 10^6 TLSs in a 1-GHz interval around the cavity frequency. Moreover, we choose the mean values of the probability distributions such that $\bar{\Gamma}_0 = |\langle\sigma_z\rangle_{\mathrm{th}}|\, P_0\langle g_i^2\rangle$, $\bar{\Gamma}_2 = \langle\Gamma_{2,i}\rangle$, and $\overline{n_s^{-1}} = \langle 4g_i^2/\Gamma_{1,i}\Gamma_{2,i}\rangle$ match the values fitted with our model on the experimental data of Fig. 3.

The expected frequency shift and damping are then computed on a regular grid of pump detuning and intracavity power by summing the contribution of individual TLSs using Eq. (2). The resulting graph is represented in Fig. 4, together with a fit using the analytic Eqs. (3) and (4). We observe a very good agreement between the fits and the values calculated with the simulations; the fitted values of Γ_0, Γ_2, and n_s^{-1} match to within 15% of the average values $\bar{\Gamma}_0, \bar{\Gamma}_2$, and $\overline{n_s^{-1}}$ of the distributions sampled in the Monte Carlo simulation. This indicates that although the Eqs. (3) and (4) were rigorously derived with the assumption of a unique value of g^2, Γ_1 and Γ_2, they well describe the effect

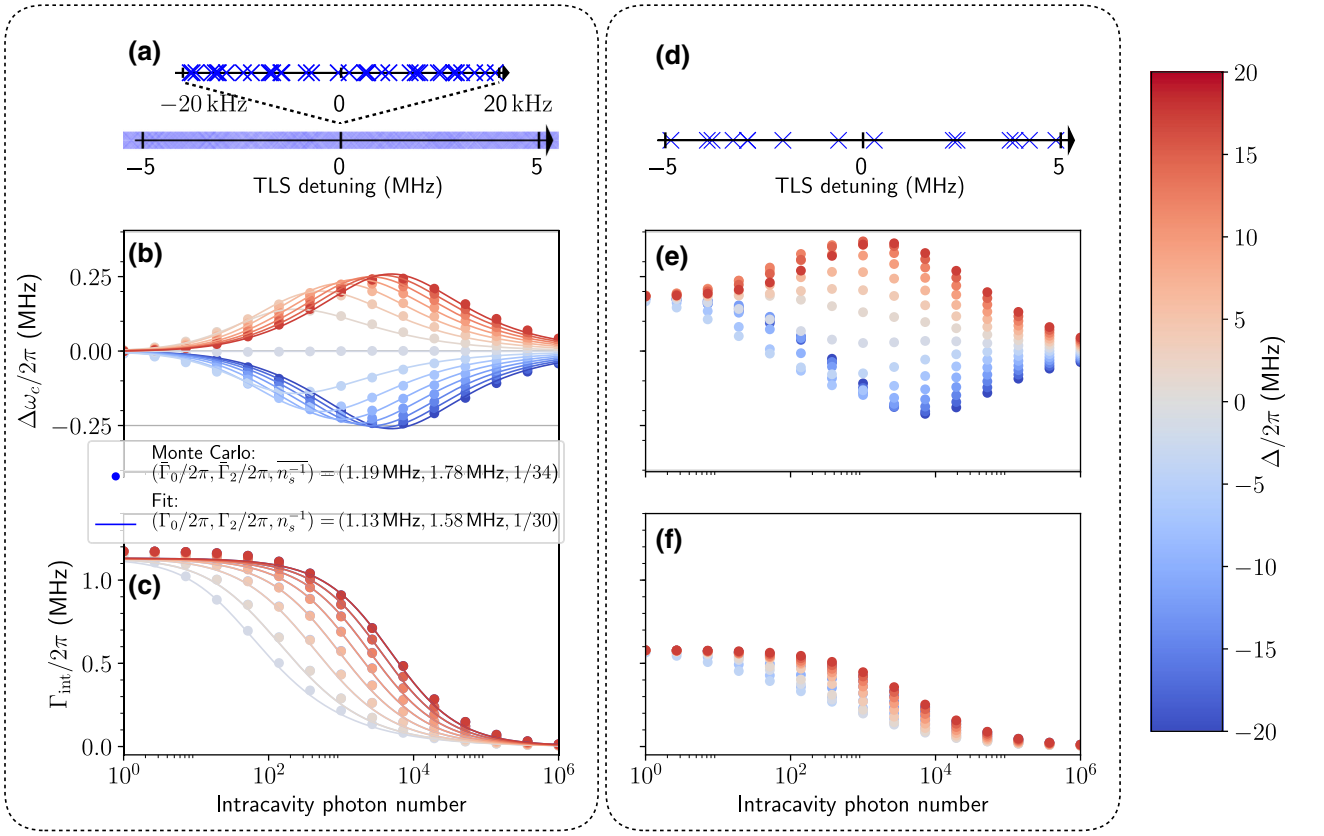

FIG. 4. (Left) Numerical validation of the model: the points in (b),(c) are the frequency shifts and dampings calculated with a Monte Carlo simulation for various pump power and detuning. The TLS frequencies are sampled from a flat distribution of density $P_0/2\pi = 1\ \mathrm{kHz}^{-1}$. A 10-MHz fragment of the sampled TLS frequencies is visible as a collection of blue crosses in (a), as well as an enlargement of a 40-kHz-wide region. The average values $(\bar{\Gamma}_0, \bar{\Gamma}_2, \overline{n_s^{-1}})$ of the sampled population (see legend) match the values obtained with the experimental fit of Fig. 3. The full lines are fits with Eqs. (3) and (4) (fitted parameters are also indicated in the legend). (Right) Random sampling effects at low TLS density: the points in (e),(f) are the typical Monte Carlo results for the same parameters as in (b),(c), except for a lower spectral density $P_0/2\pi = 1\ \mathrm{MHz}^{-1}$. In this particular realization, the reduced damping and positive frequency shift at low pump power results from a deficit of TLSs on the low-frequency side of the cavity [see sampled TLS frequencies over a 10-MHz fragment in (d)].

of a nonuniform TLS bath, provided the fitted values are interpreted as average values over the TLS distribution.

2. Effect of random sampling

Our model is insensitive to the spectral density of TLSs: the scaling $(P_0, g, \Gamma_1) \rightarrow (\alpha P_0, \alpha^{-1/2} g, \alpha \Gamma_1)$ with α an arbitrary positive number, leaves the parameters Γ_0, Γ_2, n_s unchanged. However, the smaller the density P_0, the smaller the number of resonant TLSs that will contribute to the complex frequency pull. When only a handful of TLSs contribute to the effect, we observe the signatures of the random sampling in the Monte Carlo simulation. Figures 4(e) and 4(f) show the typical shape of $\Delta\omega_c(\bar{n}, \Delta)$ and $\Gamma_{\text{int}}(\bar{n}, \Delta)$ for a TLS density as low as 1 MHz^{-1}. We observe an asymmetry in the frequency shift of the resonator: at low pump power, the frequency shift is mainly governed by the few TLSs that are located within a frequency difference Γ_2 from the resonator. An excess on one side of the cavity leads to a constant shift of the cavity frequency. On the other hand, in the large pump power limit, the cavity recovers its unshifted frequency since all the TLSs in a large frequency span around the cavity are saturated. Depending on the particular frequencies of the TLSs close to the cavity resonance, the low-power shift can be either towards low or high frequency. These effects have not been observed in our experiments, and we thus conclude that the TLS density $P_0/2\pi \gg 1$ MHz^{-1}. This result is consistent with other work from the literature [38], that found a typical surface density for resonant TLS of approximately 1 μm^{-2} (resonant TLSs are those with a detuning $|\omega_{q,i} - \omega_c| \lesssim \Gamma_2$, that contribute significantly to the low-power damping effect). With this estimate, we can infer that approximately 5000 TLSs contribute to the resonator shifts, or equivalently, a frequency density $P_0/2\pi$ in the kHz range.

V. MEASUREMENT RESULTS

To evaluate the dispersion in the parameters estimated by our technique, we repeat the fit presented in Fig. 3 on various resonators. Out of the ten resonators fabricated on each of the Si/SiO_2, Si/Si_3N_4, and Si substrates, we observe three, four, and six resonances, respectively. We attribute the missing resonances to the presence of short circuits in the interdigitated capacitors.

The three parameters $(\Gamma_0, \Gamma_2, n_s)$ extracted from the fit of each operative resonator are represented as a point in the (Γ_2, Γ_0) and (n_s, Γ_0) planes in Figs. 5(a) and 5(b), respectively. The resonators fabricated on Si/SiO_2, Si/Si_3N_4, and Si substrates are represented in red, green, and blue points, respectively. For a given substrate, the standard deviation of each parameter is represented as an error bar on the corresponding plot. Table I also summarizes the values extracted and the corresponding standard deviations for the different substrate types. The large dispersion of the parameter n_s, in particular for the Si/SiO_2 and Si/Si_3N_4 substrates, is likely due to systematic errors in the calibration of $\bar{n}$. Indeed, the determination of Γ_{ext} is difficult for these largely undercoupled resonators (for some resonators, we find a contribution of the coupling to the waveguide as low as approximately 3% of the total damping). However, since this effect only corresponds to a global shift of the curves $\Delta\omega_c(\bar{n}, \Delta)$, $\Gamma_{\text{int}}(\bar{n}, \Delta)$ towards lower occupancies $\bar{n}$, the determination of Γ_0 and Γ_2 is not affected by this inaccurate calibration. The losses Γ_0 are typically higher by a factor 5 with the Si/Si_3N_4 and Si/SiO_2 substrates as compared to Si. This indicates that

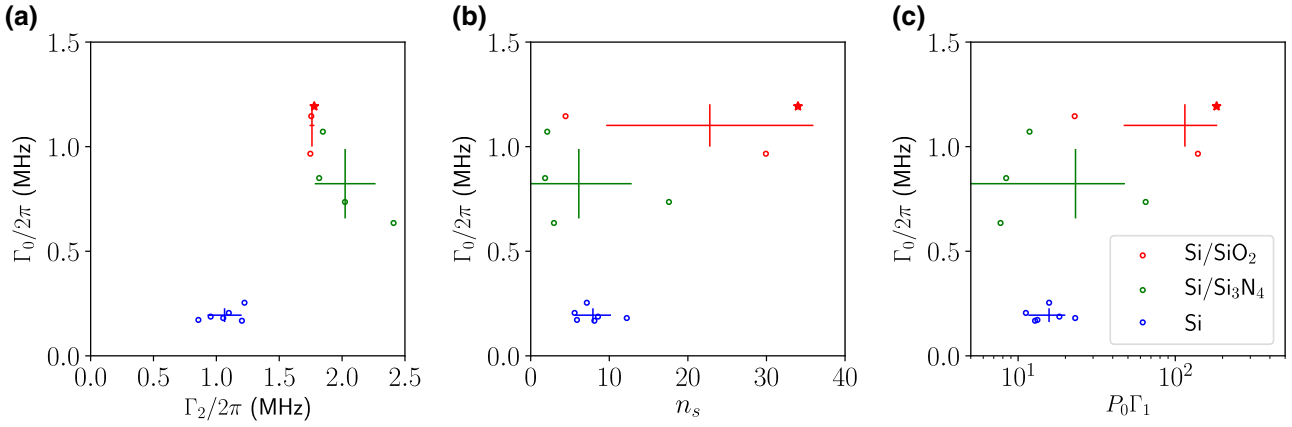

FIG. 5. Fit results: each point in the scatter plots represents the result of a fit similar to that in Figs. 3(a) and 3(b). Resonators fabricated on a Si/SiO_2, Si/Si_3N_4, and Si substrates are represented by red, green, and blue points, respectively. The coordinates (Γ_0, Γ_2) and (Γ_0, n_s) extracted on each sample are represented in (a) and (b), respectively. The same data points are represented in the $(P_0\Gamma_1, \Gamma_0)$ plane in (c), see text for details. The mean and standard deviation of each ensemble is represented as thick crosses in each of the plots. The starred data point is the result of the fit presented in Figs. 3(a) and 3(b).

TABLE I. Extracted parameters of the TLS bath for the three types of substrates. The confidence intervals are the standard deviation of the measurement clusters.

Type of wafer	$\Gamma_0/2\pi$ (MHz)	$\Gamma_2/2\pi$ (MHz)	n_s (ph)	$P_0\Gamma_1$	Q(330 mK)	Q(0 K)
Si/SiO_2	1.1 ± 0.098	1.76 ± 0.013	22.8 ± 13	115 ± 68	6800 ± 400	3300 ± 100
Si/Si_3N_4	0.823 ± 0.16	2.02 ± 0.24	6.12 ± 6.6	23.2 ± 24	7400 ± 1300	3000 ± 500
Si	0.194 ± 0.029	1.07 ± 0.13	7.92 ± 2.2	15.7 ± 4	$27\,500 \pm 3000$	$10\,000 \pm 900$

most of the TLSs are indeed located in the amorphous layers SiO_2 and Si_3N_4. Moreover, we find a dephasing rate $\Gamma_2/2\pi$ in the MHz range for the three kinds of substrate, with a consistent variation from 1.07 ± 0.13 MHz for Si substrates, 1.76 ± 0.013 MHz for the SiO_2 substrates, and 2.02 ± 0.24 MHz for the Si_3N_4 layers. This points towards different TLS microscopic nature in the various materials. Even though the TLS spectral density P_0 cannot be resolved by our technique, a *normalized* TLS spectral density $P_0\Gamma_1 = 4\Gamma_0 n_s/\Gamma_2|\langle\boldsymbol{\sigma}_z\rangle_{\text{th}}|$ can be calculated from the fitted parameters $(\Gamma_0, \Gamma_2, n_s)$. Figure 5(c) represents the same experimental points as in Figs. 5(a) and 5(b) in the $(P_0\Gamma_1, \Gamma_0)$ plane. For the three substrate types the normalized TLS spectral density is comprised between approximately 10 and approximately 200 TLSs per intrinsic linewidth. As for the parameter n_s, the relatively large scatter observed for the Si/Si_3N_4 and Si/SiO_2 substrates results from the poor determination of Γ_{ext} for these resonators. The lowest values are found on the Si and Si/Si_3N_4 substrates and the largest values on the Si/SiO_2 substrates. The low spectral density of TLSs on the Si/Si_3N_4 (comparable to the bare Si substrate) is likely due to the small thickness of the amorphous Si_3N_4 layer on these samples: the TLSs contributing to the damping are relatively rare, but strongly coupled to the resonator due to their proximity to the interdigitated capacitor.

The low-power internal quality factor $Q(330\text{ mK}) = \omega_c/\Gamma_0$, and the quality factor extrapolated at zero temperature and zero pump power $Q(0\text{ K}) = Q(330\text{ mK})\,|\langle\boldsymbol{\sigma}_z\rangle_{\text{th}}|$ is also presented in separate columns. The relatively low value of approximately 10^4 even for the samples fabricated on Si is likely due to the unusually small pitch of the interdigitated capacitors studied here [35], along with the absence of a chemical surface treatment prior to metal deposition [27].

Although recent experiments conducted on state-of-the-art high-Q resonators have seen evidence of TLS-TLS interactions in the spectrum of resonator frequency fluctuations [39,40], or on the power dependence of the damping rate in single-tone experiments [38], we do not observe such signatures in our experiments. In particular, the generalized tunneling model proposed in Ref. [41] predicts a logarithmic dependence of the resonator damping as a function of $\bar{n}$. The absence of such a signature in the samples fabricated on amorphous substrates such as Si/SiO_2 or Si/Si_3N_4 is not surprising as the density of TLSs in bulk amorphous material is too low to induce strong coupling between neighboring TLSs [41]. On the other hand, the dominating TLSs for the Si substrates are likely located at the oxide interface layers and should thus induce the same nontrivial power dependence of the damping rate. The discrepancy between our experiment and these recent works is probably due to the lack of chemical surface treatment prior to metal deposition in our sample processing. However, extending our simple model to the case of interacting TLSs could provide useful insight on the physics of these complex systems. In particular, the two-tone experiment demonstrated here may be useful to test some of the underlying hypotheses of the generalized tunneling model, such as a temperature-dependent dephasing rate of the TLSs [41].

VI. CONCLUSION

In conclusion, we present an experimental method to characterize the nonlinear properties of a TLS bath—the dominant loss channel of planar superconducting resonators. The method is applied to lumped-element resonators that have been specifically optimized to confine the electric field in a small region around the substrate surface. By selectively saturating a fraction of the TLSs that are resonant with a detuned-pump field, and simultaneously measuring the cavity spectrum with a weak probe field, we observe clear signatures of "spectral hole burning" in the TLS frequency distribution. The details of the evolution of the resonance frequencies and damping as a function of the pump detuning can be used to infer physical properties of the bath, such as its average dephasing rate Γ_2. This technique requires only standard microwave equipment and it is readily applicable to a large range of microwave resonators. Beyond their interest for the investigation of amorphous materials, the experimental signatures reported in this work can be used as a method to unambiguously identify the precise contribution of the TLS bath to the total resonator loss, and thus gives a useful insight into the design and optimization of superconducting cavities.

Furthermore, the physical situation considered here is ubiquitous in parametrically coupled systems where a particular interaction is activated by a strong pump field detuned with respect to the resonant-mode frequency. This is notably the case in reservoir engineering, where the

mode of interest inherits a nontrivial dissipation mechanism from the parametric coupling to an intentionally low-Q microwave mode [42]. In this regime, the coupled dynamics of the resonant mode and TLS bath have to be carefully studied since pump photons can be scattered to the resonator via the interaction with TLSs, leading to an effective heating process. This phenomenon is currently under theoretical investigation [43] and its characterization, which requires a quantum-limited readout to resolve the associated fluctuations, will be the subject of future work.

ACKNOWLEDGMENTS

The authors would like to thank Paolo Forni and Alain Sarlette for insightful discussions, Takis Kontos for his help with the Niobium deposition facility, Xu (Sundae) Chen, Leo Morel, and Leonhard Neuhaus for early developments. This work is supported by a Starting Grant from "Agence Nationale pour la Recherche" QuNaT (ANR-14-CE26-0002). E.F. is funded by a Junior research chair from the LabEX ENS-ICFP: ANR-10-LABX-0010/ANR-10-IDEX-0001-02 PSL*. E.I. acknowledges support from the European Union's Horizon 2020 Programme for Research and Innovation under Grant Agreement No. 722923 (Marie Curie ETN – OMT). S.C. is supported by the Grant ANR ExSqueez (ANR-15-CE30-0014).

APPENDIX A: MAXWELL-BLOCH EQUATIONS IN THE PRESENCE OF DEPHASING

The interaction of a single TLS with the cavity is described by the Jaynes-Cummings Hamiltonian (in a frame rotating at the pump frequency ω_p):

$$H = \hbar(\omega_p - \omega_c)\mathbf{a}^\dagger\mathbf{a} + \frac{\hbar(\omega_p - \omega_q)}{2}\boldsymbol{\sigma}_z + i\hbar g(\mathbf{a}^\dagger\boldsymbol{\sigma} - \mathbf{a}\boldsymbol{\sigma}^\dagger) + i\hbar J\left(\mathbf{a}^\dagger - \mathbf{a}\right),$$

where $J = a_{\text{in}}\Gamma_{\text{ext}}/\sqrt{2}$ is supposed to be real without loss of generality (the factor $\sqrt{2}$ accounts for a "hanger-type" waveguide coupling). The dissipation is described by the Lindblad equation:

$$\frac{d\rho}{dt} = -\frac{i}{\hbar}[\mathbf{H},\rho] + \Gamma_{\uparrow\downarrow}(n_{\text{th}}+1)\mathcal{D}_{\boldsymbol{\sigma}}(\rho) + \frac{\Gamma_\phi}{2}\mathcal{D}_{\boldsymbol{\sigma}_z}(\rho) + \Gamma_{\uparrow\downarrow}n_{\text{th}}\mathcal{D}_{\boldsymbol{\sigma}^\dagger}(\rho) + \Gamma_{\text{ext}}\mathcal{D}_{\mathbf{a}}(\rho),$$

with $n_{\text{th}} = 1/(e^{\hbar\omega/kT}-1)$ the occupation number of the TLS, Γ_{ext} the damping of the cavity in the absence of TLS, Γ_ϕ the eventual TLS dephasing rate, $\Gamma_{\uparrow\downarrow}$ its energy loss rate at zero temperature, and

$$\mathcal{D}_{\mathbf{A}}(\rho) = \mathbf{A}\rho\mathbf{A}^\dagger - \frac{1}{2}(\mathbf{A}^\dagger\mathbf{A}\rho + \rho\mathbf{A}^\dagger\mathbf{A}).$$

Using the formulas $\langle\mathbf{A}\rangle = \text{Tr}(\mathbf{A}\rho)$ and $(d/dt)\langle\mathbf{A}\rangle = \text{Tr}[\mathbf{A}(d/dt)\rho]$, one can compute the Maxwell-Bloch equations

$$\frac{d\langle\mathbf{a}\rangle}{dt} = \left(-i\Delta - \frac{\Gamma_{\text{ext}}}{2}\right)\langle\mathbf{a}\rangle + g\langle\boldsymbol{\sigma}\rangle + J \tag{A1}$$

$$\frac{d\langle\boldsymbol{\sigma}\rangle}{dt} = \left[-i(\omega_p - \omega_q) - \Gamma_2\right]\langle\boldsymbol{\sigma}\rangle + g\langle\mathbf{a}\boldsymbol{\sigma}_z\rangle \tag{A2}$$

$$\frac{d\langle\boldsymbol{\sigma}_z\rangle}{dt} = -2g(\langle\mathbf{a}^\dagger\boldsymbol{\sigma}\rangle + \langle\mathbf{a}\boldsymbol{\sigma}^\dagger\rangle) - \Gamma_1\left(\langle\boldsymbol{\sigma}_z\rangle - \langle\boldsymbol{\sigma}_z\rangle_{\text{th}}\right), \tag{A3}$$

where we define $\Gamma_2 = (\Gamma_{\uparrow\downarrow}/2)(1+2n_{\text{th}}) + \Gamma_\phi$, $\Gamma_1 = \Gamma_{\uparrow\downarrow}(1+2n_{\text{th}})$, $\langle\boldsymbol{\sigma}_z\rangle_{\text{th}} = -1/(1+2n_{\text{th}}) = -\tanh(\hbar\omega/2k_BT)$ and $\Delta = \omega_p - \omega_c$.

APPENDIX B: FULL DERIVATION OF THE MODEL

To transform this system [(A1), (A2), and (A3)] into a closed set of equations, we neglect the correlations and factorize the products $\langle\mathbf{a}\boldsymbol{\sigma}_z\rangle = \langle\mathbf{a}\rangle\langle\boldsymbol{\sigma}_z\rangle$, $\langle\mathbf{a}^\dagger\boldsymbol{\sigma}\rangle = \langle\mathbf{a}^\dagger\rangle\langle\boldsymbol{\sigma}\rangle$, and $\langle\mathbf{a}\boldsymbol{\sigma}^\dagger\rangle = \langle\mathbf{a}\rangle\langle\boldsymbol{\sigma}^\dagger\rangle$. Moreover, we decompose the mean values into semiclassical stationary and modulated components $\langle\mathbf{a}\rangle = \alpha + \delta\alpha(t)e^{-i\Delta t}$, $\langle\boldsymbol{\sigma}\rangle = \sigma_0 + \delta\sigma(t)e^{-i\Delta t}$, $\langle\boldsymbol{\sigma}_z\rangle = \sigma_{z0}$, and with $\delta\alpha(t)$ and $\delta\sigma(t)$ slowly varying complex functions. The equations for the stationary components then read

$$0 = (-i\Delta - \Gamma_{\text{ext}}/2)\alpha + g\sigma_0 + J, \tag{B1}$$

$$0 = [-i(\omega_p - \omega_q) - \Gamma_2]\sigma_0 + g\alpha\sigma_{z0}, \tag{B2}$$

$$0 = -2g(\alpha^*\sigma_0 + \alpha\sigma_0^*) - \Gamma_1(\sigma_{z0} - \langle\boldsymbol{\sigma}_z\rangle_{\text{th}}). \tag{B3}$$

From Eq. (B2), we get

$$\sigma_0 = \frac{g\alpha\sigma_{z0}}{i(\omega_p - \omega_q) + \Gamma_2}, \tag{B4}$$

and from Eq. (B3), we obtain the population imbalance resulting from the saturation of the transition by the pump field

$$\sigma_{z0} = \langle\boldsymbol{\sigma}_z\rangle_{\text{th}}\left[1 - \frac{\Gamma_2^2\bar{n}/n_s}{(\omega_q - \omega_p)^2 + \Gamma_2^2(1+\bar{n}/n_s)}\right], \tag{B5}$$

where $\bar{n} = |\alpha|^2$ is the mean photon number in the cavity and $n_s^{-1} = 4g^2/\Gamma_1\Gamma_2$ the number of photons required to

saturate the TLS transition. We then solve for the modulated parts by adiabatically eliminating the TLS dynamic ($d\delta\sigma/dt = 0$). From Eq. (A1), we obtain

$$\dot{\delta\alpha} = -\Gamma_{\text{ext}}\delta\alpha/2 + g\delta\sigma, \tag{B6}$$

and from Eq. (A2)

$$\delta\sigma = \frac{g\sigma_{z0}\delta\alpha}{-i(\omega_c - \omega_q) - \Gamma_2}. \tag{B7}$$

By substituting Eq. (B7) into Eq. (B6), we obtain

$$\dot{\delta\alpha} = \left[-\Gamma_{\text{ext}}/2 + \frac{g^2\sigma_{z0}}{i(\omega_c - \omega_q) + \Gamma_2}\right]\delta\alpha. \tag{B8}$$

Hence, the complex frequency pull is given by

$$\delta\omega = \frac{g^2\sigma_{z0}}{(\omega_q - \omega_c) + i\Gamma_2}. \tag{B9}$$

In turn, the population difference $\langle\boldsymbol{\sigma}_z(\omega_q)\rangle$ of a single TLS induces a shift of the complex cavity frequency [18]

$$\delta\omega = \frac{g^2\langle\boldsymbol{\sigma}_z(\omega_q)\rangle}{\omega_q - \omega_c + i\Gamma_2}. \tag{B10}$$

We also compute the total frequency shift and damping by summing the individual contributions of all the TLSs. If we assume a homogeneous distribution of frequencies of the TLS, with a density P_0, we have the following:

$$\begin{aligned}\delta\omega_c &= \int_{-\infty}^{\infty} d\omega_q \frac{P_0}{2\pi}\frac{g^2\sigma_{z0}}{\omega_q - \omega_c + i\Gamma_2} \\ &= \int \langle\boldsymbol{\sigma}_z\rangle_{\text{th}}\left[1 - \frac{\Gamma_2^2\bar{n}/n_s}{(\omega_q - \omega_p)^2 + \Gamma_2^2(1 + \bar{n}/n_s)}\right] \\ &\quad\times \frac{P_0 g^2}{(\omega_q - \omega_c) + i\Gamma_2}\frac{d\omega_q}{2\pi}.\end{aligned}$$

This integral can be interpreted as the convolution product

$$\begin{aligned}\delta\omega_c(\Delta) &= \langle\boldsymbol{\sigma}_z\rangle_{\text{th}} P_0 g^2 \\ &\quad\times \left\{\left[1 - \frac{\Gamma_2^2\bar{n}/n_s}{\omega^2 + \Gamma_2^2(1 + \bar{n}/n_s)}\right] \otimes \frac{1}{\omega + i\Gamma_2}\right\}(\Delta).\end{aligned}$$

Using standard Fourier transforms and the convolution theorem, we derive the expression

$$\begin{aligned}\delta\omega_c &= -P_0 g^2\langle\boldsymbol{\sigma}_z\rangle_{\text{th}}/2 \\ &\quad\times \left[i + \frac{\bar{n}/n_s}{\sqrt{1 + \bar{n}/n_s}}\frac{1}{\Delta/\Gamma_2 + i\left(1 + \sqrt{1 + \bar{n}/n_s}\right)}\right].\end{aligned}$$

The real and double-imaginary parts of this expression, given by formula (3) and (4), correspond to the frequency shift and damping induced by the TLS bath.

APPENDIX C: PHOTON-NUMBER CALIBRATION

The intracavity photon number at cryogenic temperature can be precisely quantified with the calibration of the total attenuation required for signal thermalization. To achieve this, we perform a separate experiment shown in Fig. 6(a) where a temperature-controlled 50-Ω termination is placed instead of the sample.

The emitted Johnson-Nyquist noise is used as a calibrated signal to extract the gain of the amplification chain G. The power spectral density measured by a spectrum analyzer depends on the temperature of the 50-Ω resistor according to $S[\omega, T] = G\{\hbar\omega_c[\exp(\hbar\omega_c/k_B T - 1)]^{-1} + S_{\text{amp}}\}$, where S_{amp} is the spectral noise density added by the amplification chain. The measured power spectral density is shown in Fig. 6(b) as a function of the temperature of the 50-Ω termination, the temperature is cycled up and down with a 5-min thermalization time for each value. The temperature sweep enables us to separate the contribution of the Johnson-Nyquist noise from the noise added from the amplification chain. Moreover, a probe is added to track slow drift of the gain of the amplification chain during the calibration. We obtain an amplification chain gain of $G = 61.8$ dB and an added noise corresponding to $S_{\text{amp}} = k_B \times 4.4$ K in agreement with the specification of the HEMT amplifier. Assuming that the amplification chain remains unchanged with respect to the setup presented in Fig. 2(a) of the main text, we are able to extract the total attenuation of the thermalization chain of 52 dB and therefore infer the photon flux at the input of the superconducting resonator $|a_{\text{in}}|^2$. Thus, the intracavity photon number can be extracted according to the following equation:

$$\bar{n} = \frac{2\Gamma_{\text{ext}}|a_{\text{in}}|^2}{\Gamma_{\text{tot}}^2 + 4\Delta^2}, \tag{C1}$$

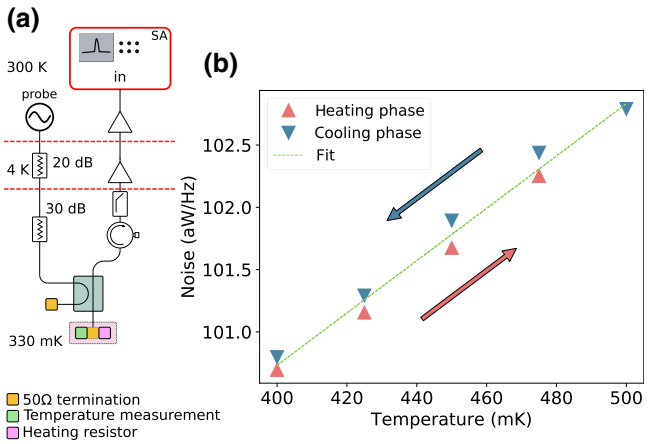

FIG. 6. (a) Setup used for the calibration of the amplification and attenuation chain. SA, spectrum analyzer. (b) Experimental results, for increasing and decreasing temperatures, with added fit.

where the coupling rate Γ_{ext}, the total decay rate Γ_{tot}, and the cavity detuning Δ are extracted from experimental fits such as those presented in Fig. 2(c) of the main text.

[1] J. Sauvageau and D. Macdonald, Superconducting kinetic inductance bolometer, IEEE Trans. Magn. **25**, 1331 (1989).

[2] M. D. Audley, R. L. Kelley, and G. L. Rawley, A prototype kinetic inductance thermometer for x-ray calorimetry, J. Low Temp. Phys. **93**, 245 (1993).

[3] A. Roy and M. Devoret, Introduction to parametric amplification of quantum signals with josephson circuits, C.R. Phys. **17**, 740 (2016).

[4] J.-D. Pillet, E. Flurin, F. Mallet, and B. Huard, A compact design for the josephson mixer: The lumped element circuit, Appl. Phys. Lett. **106**, 222603 (2015).

[5] A. Blais, R.-S. Huang, A. Wallraff, S. M. Girvin, and R. J. Schoelkopf, Cavity quantum electrodynamics for superconducting electrical circuits: An architecture for quantum computation, Phys. Rev. A **69**, 062320 (2004).

[6] I. Rau, G. Johansson, and A. Shnirman, Cavity quantum electrodynamics in superconducting circuits: Susceptibility at elevated temperatures, Phys. Rev. B **70**, 054521 (2004).

[7] A. Wallraff, D. Schuster, A. Blais, L. Frunzio, R.-S. Huang, J. Majer, S. Kumar, S. Girvin, and R. Schoelkopf, Strong coupling of a single photon to a superconducting qubit using circuit quantum electrodynamics, Nature **461**, 162 (2004).

[8] A. André, D. DeMille, J. M. Doyle, M. D. Lukin, S. E. Maxwell, P. Rabl, R. J. Schoelkopf, and P. Zoller, A coherent all-electrical interface between polar molecules and mesoscopic superconducting resonators, Nat. Phys. **2**, 636 (2006).

[9] J. Teufel, T. Donner, L. Dale, J. Harlow, M. S. Allman, K. Cicak, A. J. Sirois, J. D. Whittaker, K. W. Lehnert, and R. W. Simmonds, Sideband cooling of micromechanical motion to the quantum ground state, Nature **475**, 359 (2011).

[10] L. Toth, N. R. Bernier, A. Nunnenkamp, A. K. Feofanov, and T. J. Kippenberg, A dissipative quantum reservoir for microwave light using a mechanical oscillator, Nature **13**, 787 (2017).

[11] Y. Tabuchi, S. Ishino, T. Ishikawa, R. Yamazaki, K. Usami, and Y. Nakamura, Hybridizing Ferromagnetic Magnons and Microwave Photons in the Quantum Limit, Phys. Rev. Lett. **113**, 083603 (2014).

[12] Y. Tabuchi, S. Ishino, A. Noguchi, T. Ishikawa, R. Yamazaki, K. Usami, and Y. Nakamura, Coherent coupling between a ferromagnetic magnon and a superconducting qubit, Science **349**, 405 (2015).

[13] H. Wang, M. Hofheinz, J. Wenner, M. Ansmann, R. C. Bialczak, M. Lenander, E. Lucero, M. Neeley, A. D. O'Connell, D. Sank, M. Weides, A. N. Cleland, and J. M. Martinis, Improving the coherence time of superconducting coplanar resonators, Appl. Phys. Lett. **95**, 233508 (2009).

[14] J. Gao, M. Daal, J. M. Martinis, A. Vayonakis, J. Zmuidzinas, B. Sadoulet, B. A. Mazin, P. K. Day, and H. G. Leduc, A semiempirical model for two-level system noise in superconducting microresonators, Appl. Phys. Lett. **92**, 212504 (2008).

[15] T. Lindström, J. E. Healey, M. S. Colclough, C. M. Muirhead, and A. Y. Tzalenchuk, Properties of superconducting planar resonators at millikelvin temperatures, Phys. Rev. B **80**, 132501 (2009).

[16] S. T. Skacel, C. Kaiser, S. Wuensch, H. Rotzinger, A. Lukashenko, M. Jerger, G. Weiss, M. Siegel, and A. V. Ustinov, Probing the density of states of two-level tunneling systems in silicon oxide films using superconducting lumped element resonators, Appl. Phys. Lett. **106**, 022603 (2015).

[17] J. M. Sage, V. Bolkhovsky, W. D. Oliver, B. Turek, and P. B. Welander, Study of loss in superconducting coplanar waveguide resonators, J. Appl. Phys. **109**, 063915 (2011).

[18] N. Kirsh, E. Svetitsky, A. L. Burin, M. Schechter, and N. Katz, Revealing the nonlinear response of a tunneling two-level system ensemble using coupled modes, Phys. Rev. Mater. **1**, 012601 (2017).

[19] J. Lisenfeld, G. J. Grabovskij, C. Müller, J. H. Cole, G. Weiss, and A. V. Ustinov, Observation of directly interacting coherent two-level systems in an amorphous material, Nat. Commun. **6**, 6182 (2015).

[20] B. Sarabi, A. N. Ramanayaka, A. L. Burin, F. C. Wellstood, and K. D. Osborn, Projected Dipole Moments of Individual Two-Level Defects Extracted Using Circuit Quantum Electrodynamics, Phys. Rev. Lett. **116**, 167002 (2016).

[21] A. D. O'Connell, M. Ansmann, R. C. Bialczak, M. Hofheinz, N. Katz, E. Lucero, C. McKenney, M. Neeley, H. Wang, E. M. Weig, A. N. Cleland, and J. M. Martinis, Microwave dielectric loss at single photon energies and millikelvin temperatures, Appl. Phys. Lett. **92**, 112903 (2008).

[22] M. S. Khalil, F. C. Wellstood, and K. D. Osborn, Loss dependence on geometry and applied power in superconducting coplanar resonators, IEEE Trans. Appl. Supercond. **21**, 879 (2011).

[23] M. R. Vissers, J. S. Kline, J. Gao, D. S. Wisbey, and D. P. Pappas, Reduced microwave loss in trenched superconducting coplanar waveguides, Appl. Phys. Lett. **100**, 082602 (2012).

[24] H. Paik and K. D. Osborn, Reducing quantum-regime dielectric loss of silicon nitride for superconducting quantum circuits, Appl. Phys. Lett. **96**, 072505 (2010).

[25] J. Wenner, R. Barends, R. C. Bialczak, Y. Chen, J. Kelly, E. Lucero, M. Mariantoni, A. Megrant, P. J. J. O'Malley, D. Sank, A. Vainsencher, H. Wang, T. C. White, Y. Yin, J. Zhao, A. N. Cleland, and J. M. Martinis, Surface loss simulations of superconducting coplanar waveguide resonators, Appl. Phys. Lett. **99**, 113513 (2011).

[26] C. M. Quintana *et al.*, Characterization and reduction of microfabrication-induced decoherence in superconducting quantum circuits, Appl. Phys. Lett. **105**, 062601 (2014).

[27] A. Bruno, G. D. Lange, S. Asaad, K. L. V. D. Enden, N. K. Langford, and L. Dicarlo, Reducing intrinsic loss in superconducting resonators by surface treatment and deep etching of silicon substrates, Appl. Phys. Lett. **182601**, 4 (2015).

[28] G. Calusine, A. Melville, W. Woods, R. Das, C. Stull, V. Bolkhovsky, D. Braje, D. Hover, D. K. Kim, X. Miloshi, D. Rosenberg, A. Sevi, J. L. Yoder, E. Dauler, and W. D. Oliver, Analysis and mitigation of interface losses in

trenched superconducting coplanar waveguide resonators, Appl. Phys. Lett. **112**, 062601 (2018).

[29] Z. Leghtas, S. Touzard, I. M. Pop, A. Kou, B. Vlastakis, A. Petrenko, K. M. Sliwa, A. Narla, S. Shankar, M. J. Hatridge, M. Reagor, L. Frunzio, R. J. Schoelkopf, M. Mirrahimi, and M. H. Devoret, Confining the state of light to a quantum manifold by engineered two-photon loss, Science **347**, 853 (2015).

[30] R. Lescanne, S. Deléglise, E. Albertinale, U. Réglade, T. Capelle, E. Ivanov, T. Jacqmin, Z. Leghtas, and E. Flurin, Detecting itinerant microwave photons with engineered non-linear dissipation, arXiv:1902.05102 [quant-ph] (2019).

[31] T. Douce, M. Stern, N. Zagury, P. Bertet, and P. Milman, Coupling a single nitrogen-vacancy center to a superconducting flux qubit in the far-off-resonance regime, Phys. Rev. A **92**, 052335 (2015).

[32] P. Haikka, Y. Kubo, A. Bienfait, P. Bertet, and K. Mølmer, Proposal for detecting a single electron spin in a microwave resonator, Phys. Rev. A **95**, 022306 (2017).

[33] Q. P. Unterreithmeier, E. M. Weig, and J. P. Kotthaus, Universal transduction scheme for nanomechanical systems based on dielectric forces, Nature **458**, 1001 (2009).

[34] M. Den Otter, Approximate expressions for the capacitance and electrostatic potential of interdigitated electrodes, Sens. Actuators, A **96**, 140 (2002).

[35] K. Geerlings, S. Shankar, E. Edwards, L. Frunzio, R. J. Schoelkopf, and M. H. Devoret, Improving the quality factor of microwave compact resonators by optimizing their geometrical parameters, Appl. Phys. Lett. **100**, 192601 (2012).

[36] M. S. Khalil, M. J. A. Stoutimore, F. C. Wellstood, and K. D. Osborn, An analysis method for asymmetric resonator transmission applied to superconducting devices, J. Appl. Phys. **111**, 054510 (2012).

[37] W. Phillips, Two-level states in glasses, Rep. Prog. Phys. **50**, 1657 (1987).

[38] J. Burnett, L. Faoro, and T. Lindström, Analysis of high quality superconducting resonators: Consequences for TLS properties in amorphous oxides, Supercond. Sci. Technol. **29**, 044008 (2016).

[39] J. Burnett, L. Faoro, I. Wisby, V. L. Gurtovoi, A. V. Chernykh, G. M. Mikhailov, V. A. Tulin, R. Shaikhaidarov, V. Antonov, P. J. Meeson, and T. Lindstro, Evidence for interacting two-level systems from the 1/f noise of a superconducting resonator, Nat. Commun. **5**, 4119 (2014).

[40] L. Faoro and L. B. Ioffe, Interacting tunneling model for two-level systems in amorphous materials and its predictions for their dephasing and noise in superconducting microresonators, Phys. Rev. B **91**, 014201 (2015).

[41] L. Faoro and L. B. Ioffe, Internal Loss of Superconducting Resonators Induced by Interacting Two-Level Systems, Phys. Rev. Lett. **109**, 157005 (2012).

[42] E. Kapit, The upside of noise: Engineered dissipation as a resource in superconducting circuits, Quantum Sci. Technol. **2**, 033002 (2017).

[43] P. Forni, A. Sarlette, T. Capelle, E. Flurin, S. Deleglise, and P. Rouchon, in *57th IEEE Conference on Decision and Control, CDC 2018, Miami, FL, USA, December 17–19, 2018* (IEEE, Miami, 2018), p. 6614.